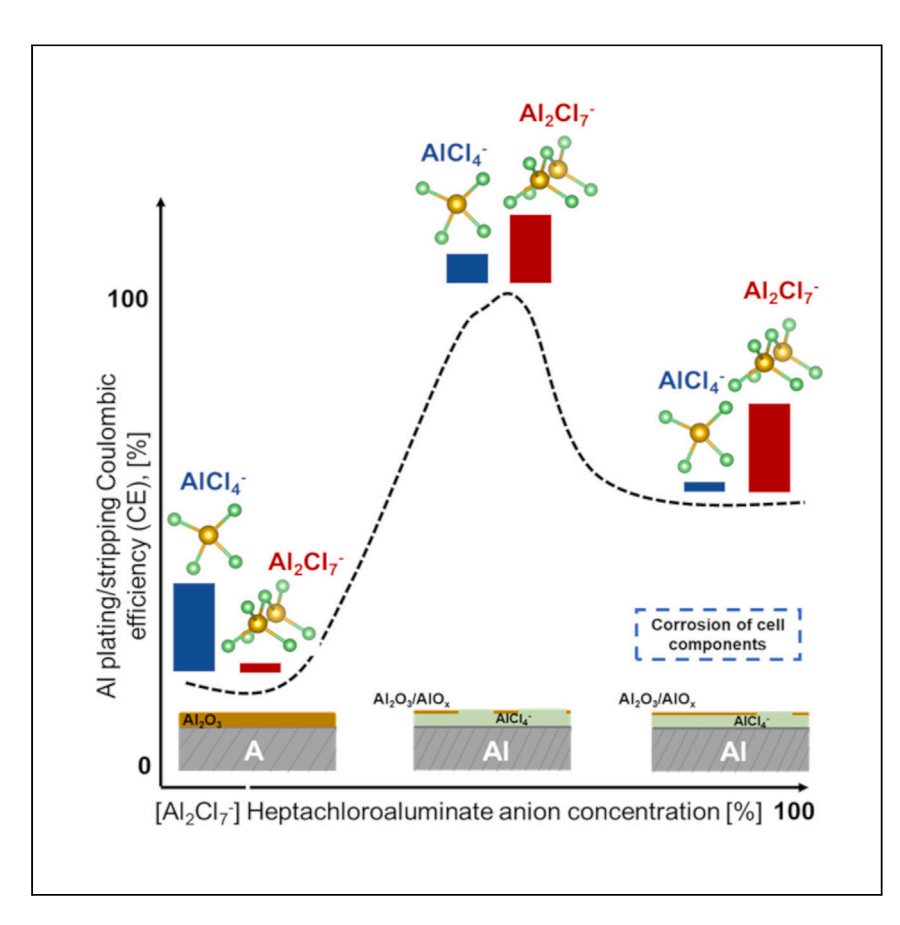


Article

Understanding the reversible electrodeposition of aluminum in low-cost room-temperature molten salts



Garcia-Mendez et al. report a molecular design approach for creating low-melting-point electrolytes with desired Lewis acidity to enable highly reversible aluminum electrodeposition and dissolution in batteries. The approach yields cost-effective, environmentally benign electrolyte alternatives to state-of-the-art imidazolium-based melts for grid storage applications.

Regina Garcia-Mendez, Jingxu Zheng, David C. Bock, ..., Kenneth J. Takeuchi, Esther S. Takeuchi, Lynden A. Archer

jkzheng@mit.edu (J.Z.) laa25@cornell.edu (L.A.A.)

Highlights

Ammonium-based electrolytes are designed with melting points below room temperature

Both AlCl₄⁻ and Al₂Cl₇⁻ have a role in controlling Al plating/ stripping reversibility

AlCl₄⁻ anions intercalate in the cathode during charging of Al|| graphite batteries

Garcia-Mendez et al., Cell Reports Physical Science 4, 101452 June 21, 2023 © 2023 The Authors. https://doi.org/10.1016/j.xcrp.2023.101452





Article

Understanding the reversible electrodeposition of aluminum in low-cost room-temperature molten salts

Regina Garcia-Mendez,^{1,2} Jingxu Zheng,^{3,4,*} David C. Bock,^{5,6} Cherno Jaye,⁷ Daniel A. Fischer,⁷ Amy C. Marschilok,^{5,6,8,9} Kenneth J. Takeuchi,^{5,6,8,9} Esther S. Takeuchi,^{5,6,8,9} and Lynden A. Archer^{1,2,3,10,*}

SUMMARY

Aluminum is the most earth-abundant metal, trivalent, and inert in ambient air; it also has a density approximately five times that of lithium at room temperature, making it attractive for cost-effective, long-duration storage in batteries. Here, we investigate structural requirements and physicochemical and transport properties of ionic liquid (IL) electrolytes thought to enable high reversibility of Al battery anodes. We find that intentionally designed, low-cost IL analogs, including ammonium-based molten salts, offer comparable Al anode reversibility to state-of-the-art imidazolium-based IL melts. A critical ratio of solvated Al-ion species is required to balance the effects of Lewis acidity needed to continuously etch native Al_2O_3 and form a stable solid electrolyte interphase on Al. Our findings open new opportunities for developing simple, cost-effective, room-temperature Al batteries that enable long-duration electrical energy storage.

INTRODUCTION

Electrochemical cells based on aluminum have been pursued for more than a decade as a promising technology for storing electrical energy at low cost. 1,2 The rationale for this interest is straightforward and manyfold. The low cost and simplicity of the battery anode and of the most often used cathode materials (a graphitic carbon sheet), mature manufacturing and recycling of Al, air stability of both anode and cathode, high volumetric energy density, and Earth crust abundance of Al (13 kWh L^{-1} for Al vs. 6, 4, and 3 kWh L^{-1} for Li, Zn, and Na, respectively, and 8% abundance for Al vs. 0.0065%, 0.0075%, and 2.3% for Li, Zn, and Na, respectively) are attributes that differentiate Al batteries from other candidates of contemporary interest. Notwithstanding these beneficial features, Al-based batteries have historically failed to live up to the promise of the chemistry for mainly two reasons. First, the highband-gap (7 eV) Al₂O₃ coating, which forms spontaneously on Al and protects it from chemical attack by atmospheric agents, passivates the metal in conventional liquid electrolytes. The result is that high overpotentials are required to plate Al during battery charging and reversible plating/stripping of Al during charge and discharge of a secondary/rechargeable Al battery is limited to a small number of specialized, typically expensive electrolytes. Second, the redox active species in these electrolytes are bulky 4-fold ($[A|X_4]^-$) and 7-fold ($[A|_2X_7]^-$) coordinated Al species, which rules out most insertion type materials as cathode candidates because reversible de-/insertion of the multivalent coordinated Al ions is difficult because of their low mobility. Here, X is most commonly a halogen.



¹Department of Chemical and Biomolecular Engineering, Cornell University, Ithaca, NY 14853,

²Cornell Energy Systems Institute, Cornell University, Ithaca, NY 14853, USA

³Department of Materials Science and Engineering, Cornell University, Ithaca, NY 14853, USA

⁴Department of Physics, Massachusetts Institute of Technology, Cambridge, MA 02129, USA

⁵Interdisciplinary Science Department, Brookhaven National Laboratory, Upton, NY 11973, USA

⁶Institute for Electrochemically Stored Energy, Stony Brook University, Stony Brook, NY 11794, USA

⁷National Synchrotron Light Source II, Brookhaven National Laboratory, Upton, NY 11973, USA

⁸Department of Chemistry, Stony Brook University, Stony Brook, NY 11794, USA

⁹Department of Materials Science and Chemical Engineering, Stony Brook University, Stony Brook, NY 11794, USA

¹⁰Lead contact

^{*}Correspondence: jkzheng@mit.edu (J.Z.), laa25@cornell.edu (L.A.A.)

https://doi.org/10.1016/j.xcrp.2023.101452





Despite these challenges, a number of studies conducted particularly in the last decade ^{1–3} have demonstrated that it is possible to create rechargeable Al batteries in 1-ethyl-3-methylimidazolium AlCl₃/EMIMCl ionic liquid (IL) electrolyte melts. Why these electrolytes are successful in enabling Al reversibility largely remains an open question. Lewis acidity, high ion mobility at the Al/electrolyte interface, and a melting point below room temperature are considered required properties of IL electrolytes. Initial analyses of the interphases formed on an Al electrode suggested, but did not confirm, that the first of these properties is important for etching away the passivating Al₂O₃ coating and enabling fast interfacial ion transport at the Al/electrolyte interface. One study reported that exposure of Al to an imidazolium-based IL electrolyte creates an ionically conducting interphase on the Al electrode that remains intact when the electrode is immersed in other electrolyte media, including aqueous electrolytes, enabling stable cycling of the Al anode for up to 50 cycles. The composition and transport properties of the ionically conducting interphase were not investigated.⁴

In considering how one might design lower-cost analogs of the IL electrolytes known to facilitate reversible plating and stripping of an Al anode, we first note that desirable IL electrolyte properties are not unique to the [EMIM] cation. The Lewis acidity is in fact controlled by the molar ratio between the IL salt ([C]+X^-) and AlCl3 (e.g., [C]+Cl^-+AlCl3 \rightarrow [C]+[AlCl4]^-). This, in turn, sets the relative concentration of electrochemically active $[AlX_4]^-$ and $[Al_2X_7]^-$ species present at room temperature. The low melting point of the AlCl3/EMIMCI (1-ethyl-3-methylimidazolium chloride) electrolyte melt, in contrast, is conventionally attributed to the large size of the imidazolium cation in comparison with the Cl^- anion; the size mismatch destabilizes the ion packing in the solid state and therefore results in a lower melting point. The key discovery that motivates the present report is that the electrolyte properties required for high Al anode reversibility in electrochemical cells are independent of the specific chemical structure of the cation species $[C]^+$. This surprising finding opens new approaches for designing chemically simpler and, thus, inexpensive electrolytes that enable highly reversible cycling of Al batteries.

Angell et al. reported that mixtures of urea, i.e., $CO(NH_2)_2$, or its derivatives and AlCl₃ produce ionic-liquid-analog electrolytes, which allow both Al plating/stripping at the anode and intercalation at some cathodes. The authors noted, however, that more pronounced and undesirable parasitic side reactions are observed in these electrolytes, ^{6,7} attributable perhaps to the higher chemical reactivity of the carbonyl group in urea, ^{8,9} in comparison with the EMIM cation containing only aromatic, imidazole ring, C–C and C–H bonds, which are in general deemed to be chemically stable. An alternative approach was reported by Yan et al., ¹⁰ whereby amorphization of a metallic anode via alloying and dealloying Li to the Al substrate lowers the Al nucleation barrier and favors Al deposition over the electron-stealing hydrogen evolution reaction (HER) in Al₂(SO₄)₃ aqueous electrolyte. Nonetheless, the authors noted that further optimization of the electrolyte is needed to broaden the voltage window of aqueous systems and fully suppress HER.

We hypothesize that simple, low-cost electrolytes designed using ammonium-based salts of broken symmetry (i.e., in which the four moieties connected to the nitrogen atom are not equivalent), can be designed to simultaneously exhibit melting points below room temperature and high solvation power for AlCl₃ and its analogs. Such electrolytes would therefore enable plating and stripping of Al inside electrochemical cells with comparable levels of reversibility as the IL melts investigated in earlier works.

Article



In this work, we demonstrate that the reversibility of Al plating and stripping, the nature of the solid electrolyte interphase it forms, and the morphological evolution during plating and stripping of Al depend sensitively and quantitatively on the ratio of $AlCl_4^-$ to $Al_2Cl_7^-$ ions in the electrolyte. The dual role played by the ions in facilitating electroreduction at the Al/electrolyte interface and in etching the resistive native alumina surface layer enables Al transport to the interface. Given that the ratio of $AlCl_4^-$ to $Al_2Cl_7^-$ ions can be preserved in room-temperature electrolytes with broken cation symmetry, highly reversible plating and stripping of Al is attained in cost-effective quaternary ammonium-based electrolyte media.

RESULTS AND DISCUSSION

Liquidus regimes at room temperature

As a first step to designing low-cost electrolytes, we consider ILs in which $[C]^+$ is a quaternary ammonium species; a variety of quaternary ammonium cations composed of short-chain alkyl groups, e.g., methyl-, and ethyl-, which are commercially available and at relatively moderate costs (\leq US\$200 per kilogram). Manipulating the symmetry of the cation offers a powerful route toward achieving low-melting-point electrolytes with the desired Lewis acidity. The simplest symmetry breaking of the nitrogen atom is achievable by replacing one alkyl group with a hydrogen atom, making it a ternary amine. The hydrogen atom breaks the perfect tetrahedron that facilitates packing and alters the symmetry of the cation from a high-order $T_{\rm d}$ point group to a low-order $C_{\rm 3v}$ point group. Even this modest change reduces the number of symmetry elements from 24 to 6. We note here that symmetry breaking 11,12 interferes with molecular packing and is an already studied approach for depressing the melting point of molecular crystals, also known as Carnelley's rule.

To evaluate this hypothesis, we studied physical and electrochemical properties of Al in electrolytes based on tetramethylammonium chloride (AlCl $_3$ /TetraMACl), triethylamine hydrochloride (AlCl $_3$ /TriEAHCl), and trimethylamine hydrochloride (AlCl $_3$ /TriMAHCl) melts, in which the symmetry of the ammonium ion is broken to progressively greater extents. As reference, we compare the studied properties with those measured using AlCl $_3$ /EMIMCl, the most frequently used IL electrolyte in Al electrochemical cells. As illustrated in Figure 1A, the measured melting points of the symmetry-broken quaternary ammonium species drop markedly with reduced symmetry of the cation; the values achieved for TriMAHCl are in fact comparable with those for EMIMCl. Significantly, we also find that Al electrodes are reversible in all of the studied electrolytes and that in Al plating/stripping experiments, the quaternary ammonium chloride-based electrolytes display high levels of reversibility (Al plating/stripping Coulombic efficiency [CE] \geq 99.3% for 1,000 cycles at practical areal capacities and current densities [1 mAh·cm $^{-2}$, 4 mA cm $^{-2}$]), which are comparable with those observed in the AlCl $_3$ /EMIMCl electrolyte.

Using 27 Al quantitative nuclear magnetic resonance (NMR), electrochemical measurements, and scanning probe microscopy, we show that plating/stripping reversibility increases with AlCl₃ concentration, with an upper limit. By probing the surface chemistry of the anodes and imaging the electrode's morphology after electrodeposition using focused ion beam scanning electron microscopy (FIB-SEM), we find that Al plating/stripping reversibility is increased by continuous etching of the Al $_2$ O $_3$ resistive interfacial layer and formation of a stable conductive solid electrolyte interphase (SEI) on the Al anode. The magnitude of the increase depends on the AlCl $_4$ 7/ Al $_2$ Cl $_7$ 7 ratio (Figure 1B), where a balance between Lewis acidity and lack of excess



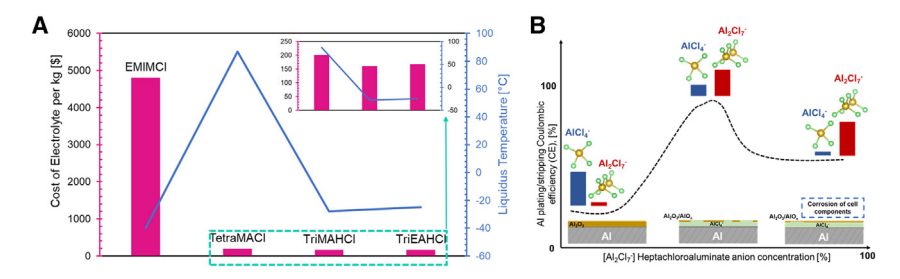


Figure 1. Rationale used in selecting ammonium-based electrolytes and how their solvation structures impact the Al anode chemistry and Al plating/stripping reversibility

(A) Effect of molecular structure and symmetry on cost and melting point of electrolytes that enable reversible stripping and plating of aluminum.

(B) Schematic illustrating the interplay between the $AICI_4^-$ -to- $AI_2CI_7^-$ ratio and the Al plating/stripping Coulombic efficiency coupled with the interphase chemistry on an Al electrode.

The concentration used for liquidus temperatures was 1.5 mol of $AlCl_3$ to 1 mol of alkylammonium/ imidazolium chloride. The costs only consider the solvent and not the salt: $AlCl_3$. The relative values in (B) for the x axis are taken from the ^{27}Al NMR measurements from Figure 3, and for the y axis from Figures 4A and S8, summarized in Table S1 and Figure S1.

corrosion of the cell components determine the critical ratio. Our results quantitatively link the concentration of solvation species in the electrolytes to Al plating/stripping reversibility. In addition, the composition and resistivity of the SEI was deconvoluted through X-ray photoelectron spectroscopy (XPS) and electrochemical impedance measurements as a function of the number of cycles.

We mapped out the concentrations of ammonium-based electrolytes that form ILs (or molten salts at room temperature) using phase diagrams obtained from differential scanning calorimetry (DSC) with heating and cooling capabilities (Figure 2). The effect of the cooling/heating rate on freezing points in AlCl₃/EMIMCI (1.5:1 in molar ratio) was evaluated to select the rate that is less dependent on the kinetics of the measurement. As seen in Figure S2, rates between 3° C min⁻¹ and 6° C min⁻¹ result in a minor change in the freezing point of the mixtures. Thus, 3° C min⁻¹ was chosen to construct phase diagrams in all systems.

The concentrations that formed molten salts at room temperature were mainly observed between the AlCl₃/salt ratios 1:1 (50 mol % AlCl₃) to 2.6:1 (72.2 mol % AlCl₃). The exception is the electrolyte system composed of the most symmetric and highest molar mass cation AlCl₃/TetraMACl, which remained in solid, crystalline form over the entire concentration range of AlCl₃ studied. These measurements are in agreement with our preliminary observations in mixing higher tetra-alkyl-based compounds with AlCl₃ (Figure S3), confirming the effect of molecular structure on the melting point and liquid ranges. ¹³ Increasing the molecular symmetry in the electrolyte, as is the case with tetra-alkyl compounds (Figure S4), promotes charge ordering and efficient packing remaining in crystalline form at room temperature. ¹⁴

Using the group contribution method (GCM) developed by Lazzús, melting temperatures (T_m) for a wide range of ILs with cation groups, including imidazolium, pyridinium, pyrrolidinium, ammonium, etc., can be estimated with an average deviation of 7%. ¹⁴ Thus, the GCM method was used to rationalize the structural effects on the thermal behavior of each system. The mathematical foundation of the GCM method is based on the principle of collinearity. T_m is a linear combination of any number of functions of the independent variables or functional groups in this case. The functional groups are divided into groups for the cation and the anion part, and the



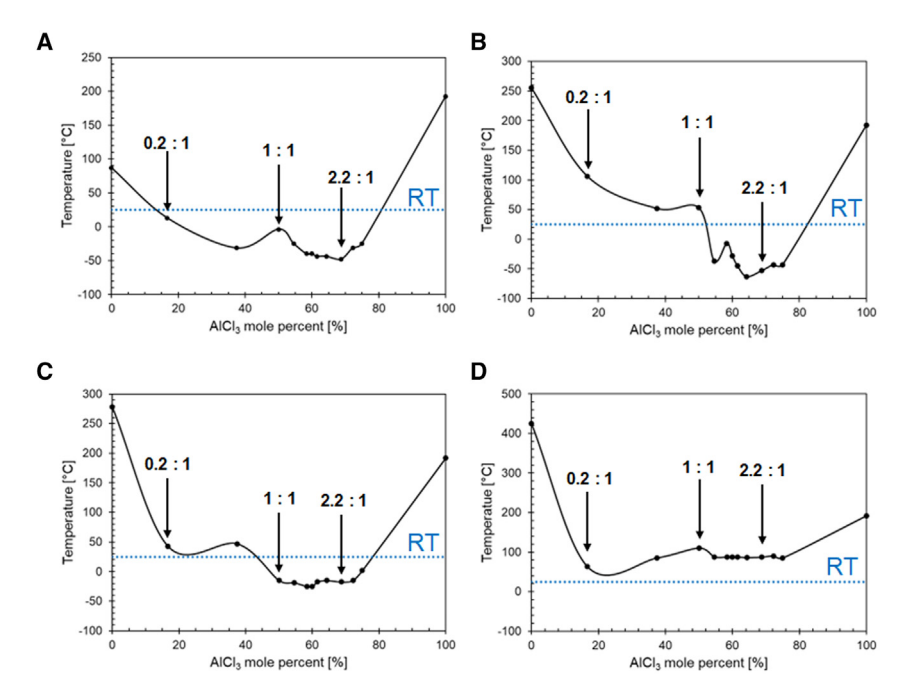


Figure 2. Phase diagrams of ammonium-based electrolytes as a function of AlCl₃ mol % (A) 1-Ethyl-3-methylimidazolium chloride (EMIMCl), (B) triethylamine hydrochloride (TriEAHCl), (C) trimethylamine hydrochloride (TriMAHCl), and (D) tetramethylammonium chloride (TetraMACl). Blue dotted line corresponds to 25°C (RT, room temperature). The ratios in each plot correspond to mole ratios between AlCl3 salt and imidazolium/alkylammonium chloride.

size, shape, and asymmetry of the cation and anion parts of each system play a role in the $T_{\rm m}$ measured. The melting point decreased as the AlCl $_3$ concentration increased due to the formation of $Al_2Cl_7^-$ anions, which are larger than $AlCl_4^-$, known to be formed in acidic compositions, i.e., when AlCl $_3$ is added in excess of the EMIMCl. $^{15-17}$ An increase in anion size led to reductions in the melting points by reducing the Coulombic attraction contributions to the lattice energy of the crystal and increasing the covalency of the ions. 13 For the cation part, length and asymmetry were more significant in determining the melting point and liquid ranges. The TriEAHCl systems having longer alkyl chains than the TriMAHCl enable higher charge delocalization, further reducing the overall charge density, and both of their asymmetries disrupt the crystal packing and reduce the crystal lattice energy, resulting in a lower melting temperature. Given that the TetraMACl system remained crystalline for all concentration ranges, it was not further explored as an electrolyte for the room-temperature Al electrochemical cells of interest here.

Anionic species identification and quantification

We next interrogated the solvation species in the ammonium-based and imidazolium-based IL electrolytes using ^{27}Al NMR from chemical shifts: 103.8 \pm 2.0 ppm for $\text{AlCl}_4^{-6,18-20}$ and 97.5 \pm 1.0 ppm for $\text{Al}_2\text{Cl}_7^{-19}$ (Figures S5–S7). There was no detectable concentration of $\text{Al}_3\text{Cl}_{10}^{}$ species, 81 ppm 21 throughout the entire AlCl_3 concentration range evaluated in this work. The spectra were fitted to quantitatively compare the relative concentration of the anionic solvation species for each sample that form molten salts at room temperature (Figure 3). Both TriMAHCI and TriEAHCI systems exhibited the same aluminum anion species as the AlCl $_3$ /EMIMCI system. Nevertheless, the ratio of each species in the electrolytes varies for each system, especially for the TriMAHCI system. Figures 3A and 3B show that from the range at which the EMIMCI



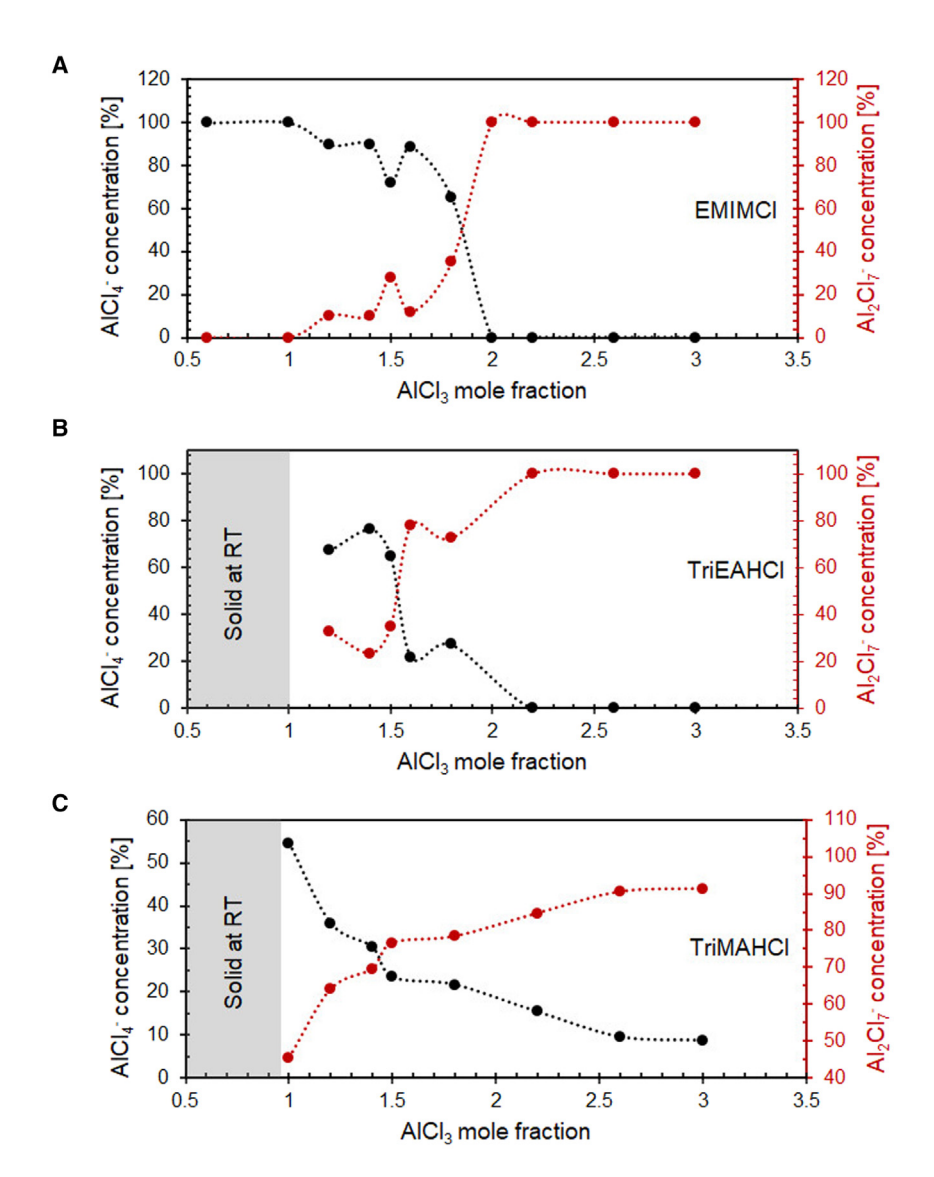


Figure 3. Percentage of $AICI_4^-$ and $AI_2CI_7^-$ in ionic liquids as a function of $AICI_3$ mole fraction, determined via quantitative ^{27}AI NMR

(A) $AICI_3/EMIMCI$ (1-ethyl-3-methyl-imidazolium chloride), (B) $AICI_3/TriEAHCI$ (triethylamine hydrochloride), and (C) $AICI_3/TriMAHCI$ (trimethylamine hydrochloride). See also Figures S4–S6.

and TriEAHCl systems form a molten salt, there is a wide range of $AlCl_4^-$ and $Al_2Cl_7^-$ concentrations that can be attained by varying the $AlCl_3$ mole fraction. These observations are consistent with previous ^{27}Al NMR studies of $AlCl_3$ /EMIMCl electrolytes. 5,22 In contrast, Figure 3C shows that the majority of the molten salts formed in the TriMAHCl system have $Al_2Cl_7^-$ as the majority species ($\geq 64\%$), i.e., all acidic.

One of the critical challenges in developing rechargeable Al batteries is the limited number of electrolytes that enable reversible Al plating/stripping at room temperature. ¹⁸ We investigated the reversibility of Al in TriMAHCI and TriEAHCI electrolytes using galvanostatic experiments in which Al was deposited on a conductive fibrillar carbon substrate. The carbon 3D-electrode architecture was chosen because it has been demonstrated to facilitate electron transport and promote strong oxygenmediated chemical bonding between Al deposits and the carbon substrate,

Article



facilitating control of deposition morphology and limiting out-of-plane Al growth in imidazolium-based electrolytes.^{3,23} Similar approaches have been used in Na-ion and Zn-ion systems, where 3D matrices or 3D fiber hosts, respectively, have been used as electrodes to enable homogeneous metal deposition.^{24,25} Scanning electron microscopy (SEM) and energy-dispersive spectroscopy (EDS) analysis of the substrate were conducted to study the chemistry of the electrodeposits. From the EDS elemental maps (Figure S8), it is evident that conformal coatings composed of Al are formed in the fibers of the carbon substrate for all systems. This finding is in agreement with the morphology observed in a prior study using 1.3:1 AlCl₃/EMIMCI.³

Aluminum electrodeposition in room-temperature molten salts

The confirmation of Al electrodeposits in the proposed systems combined with the knowledge gained via NMR spectroscopy enables detailed investigation of the electrolyte features responsible for the observed reversibility by simply varying the AlCl₄⁻ and Al₂Cl₇⁻ concentration. Prior studies reported that acidic AlCl₃/EMIMCl melts (i.e., melts in which AlCl₃ is added in excess of the EMIMCl, and for which the dominant species is Al₂Cl₇⁻) are responsible for the reversible Al deposition according to the reaction $4Al_2Cl_7^- + 3e^- \leftrightarrow Al + 7AlCl_4^{-.26}$ Al plating/stripping Coulombic efficiency (reversibility) (CE) was measured by performing galvanostatic tests on carbon 3D-electrode substrates using selected compositions of each electrolyte system. The CE of each system quantifies the percentage of Al metal that can be stripped from the Al originally plated. In these studies, three concentrations were chosen for each electrolyte; one with AlCl₄ as the dominant species, one with the Al₂Cl₇⁻ as the dominant species, and a third that consisted of a mixture of both anionic species. The electrolytes with a mixture of both anionic species, especially those with a higher concentration of Al₂Cl₇⁻ (Figure 4), showed higher reversibility for all electrolytes (Figure S9). It is noteworthy that the AlCl₃/EMIMCl mixture containing approximately 65% of AlCl₄⁻ and 35% Al₂Cl₇⁻, compared favorably with those, respectively, containing 22% and 23% of AlCl₄⁻ and 78% and 77% of Al₂Cl₇⁻ for the TriEAHCl and TriMAHCl mixtures. The Al plating/stripping CEs measured were 99.2%, 99.5%, and 99.3%, for 1.8:1 AlCl₃/EMIMCl, 1.6:1 AlCl₃/ TriEAHCl, and 1.5:1 AlCl₃/TriMAHCl, respectively, at 1 mAh cm⁻² areal capacity and 4 mA cm⁻² current density for 1,000 cycles. Interestingly, we observed that these modest changes in CE are accompanied by quite large differences in cell polarization and morphology of the electrodeposited Al. The voltage profiles in Figure 4B reveal a more stable Al stripping/plating reaction for the TriEAHCl and TriMAHCl electrolytes by a reduced overpotential that remains constant from cycles \sim 50 to 1,000, compared with the EMIMCI electrolyte. Comparable behavior was observed in Al symmetric cells (Figures S10 and S11), where CE of 99.9% was measured for both 1.5:1 AlCl₃/TriMAHCl and 1.6:1 AlCl₃/TriEAHCl at 1 mAh cm⁻² areal capacity and 4 mA cm⁻² current density for 5,000 cycles. The decrease in potential response as a function of cycling correspond to a decrease in the impedance of the interfacial layer on the Al anode and charge transfer impedance evidenced by electrochemical impedance spectroscopy (EIS) measurements (Figure S12). The intercept on the x axis at high frequencies, which corresponds to the uncompensated impedance and liquid electrolyte impedance, remains constant throughout cycling. Thus, we conclude that there is no evidence that Al is being electrodeposited in dendritic form toward the other electrode. The narrowing of the overpotential over the first 50 cycles will be explained in more detail in the next section in the context of changes in the surface chemistry of the Al anodes via XPS and X-ray absorption measurements.



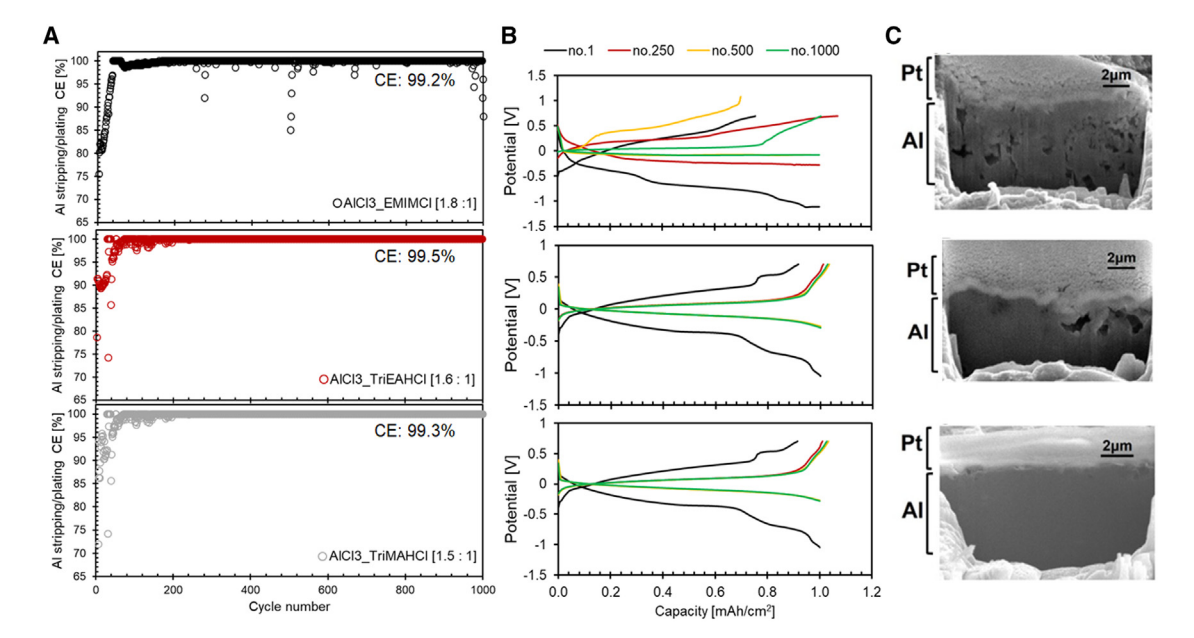


Figure 4. Electrochemical cycling behavior of Al electrodes in galvanostatic plating/stripping experiments

Data using various electrolytes: (top) 1.8:1 AlCl₃/EMIMCl; (middle) 1.6:1 AlCl₃/TriEAHCl; (bottom) 1.5:1 AlCl₃/TriMAHCl.

(A) Al plating/stripping Coulombic efficiency measured at 1 mAh cm⁻² areal capacity and 4 mA cm⁻² current density.

(B) Voltage profiles obtained during Al plating/stripping at 1 mAh cm⁻² areal capacity and 4 mA cm⁻² current density.

(C) SEM of FIB-milled cross-sections of Al anodes cycled using various electrolytes.

See also Figures S8–S13.

Representative SEM analysis on FIB-cut cross-sections of the electrodeposited Al confirmed the presence of voids near the surface and within the bulk of the anode for the EMIMCI electrolyte (Figure 4C). Evidence of voids and pitting are apparent near the surface of the electrodeposited Al in TriEAHCI. In contrast, electrodeposited Al harvested from the TriMAHCI electrolyte forms as a dense layer throughout the bulk and near the surface of the anode. Multiple areas in all electrolytes were examined to confirm that these observations are in fact quite general. Our results therefore show that ammonium-based electrolytes composed of a mixture of AlCl₄ and Al₂Cl₇, with Al₂Cl₇ as the moderate majority (\geq 70%) ionic species, facilitate higher reversibility of Al and formation of deposits with planar, dense morphologies. The mixtures with the dominant species of either AlCl₄ or Al₂Cl₇ (>65% of AlCl₄ or \geq 90% of Al₂Cl₇) comparatively underperformed in Al plating/stripping reversibility (Figure S9). The mixtures with a predominantly higher concentration of AlCl₄ showed poor reversibility, with average CE values ranging from 64.9% to 75.7% (Figures S9A and S9C).

This is a direct result of the inherent irreversibility of the predominant electrodeposition process in neutral melts: $AlCl_4^- + 3e^- \leftrightarrow Al + 4Cl_-^{-26}$ As the $Al_2Cl_7^-$ concentration increases, the Lewis acidity of the electrolytes increases. Thus, a higher Lewis acidity corresponds to a higher affinity from the electrolytes to accept a pair of electrons and form a coordinate covalent bond, resulting in electrochemical corrosion of the metal parts in the cell. This phenomenon was observed in highly acidic electrolytes ($Al_2Cl_7^- \ge 90\%$), where the charging step would extend for overly long periods, indicative of a faradic process occurring, as seen in Figure S13. Although the CE values appeared to be higher than the mixtures with high $AlCl_4^-$ concentration, upon closer examination of the potential curves electrochemical corrosion after tens of cycles was identified as the controlling process occurring within the cell.

Article



Although the $AlCl_4$ ion cannot be reduced directly at the electrode to form Al, it can affect the Al electrodeposition process through a dissociation reaction: $2AICI_4^- \leftrightarrow$ $Al_2Cl_7^- + Cl^-$. In turn, the reduction of $Al_2Cl_7^-$ leads to aluminum deposition according to the reaction: $4Al_2Cl_7^- + 3e^- \leftrightarrow Al + 7AlCl_4^{-18,27}$ A key remaining question concerns the effect of the electrolyte composition on physicochemical and transport properties. The conductivity of a material is a measure of the available charge carriers and their mobility. Ionic liquids composed entirely of ions would be expected to have high ionic conductivity values. However, ion pairing and/or ion aggregation commonly decrease the number of available charge carriers. 12 Prior work from Fannin et al.²⁸ reported ionic conductivity values at room temperature for the AICl₃/ EMIMCI system: the basic concentrations with a value of \sim 6.5 mS cm⁻¹ (presence of Cl⁻ and AlCl₄⁻ anions), neutral having a value of ~23.0 mS cm⁻¹ (presence of $AlCl_4^-$ anions), and acidic concentrations having a value of ~ 15.0 mS cm⁻¹ (presence of AlCl₄⁻ and Al₂Cl₇⁻ anions). We measured the ionic conductivity of electrolytes used in the study using a dielectric spectrometer with a temperature controller incorporated. The values measured for the EMIMCI electrolytes followed the expected trend: the neutral concentration exhibited the highest conductivity, followed by acidic concentrations, and a lower conductivity for the only basic concentration considered in this work. Both TriMAHCl and TriEAHCl electrolyte mixtures with a high concentration of AlCl₄ presented the highest conductivity values and a decrease as the concentration of Al₂Cl₇⁻ increased per ²⁷Al quantitative NMR analysis. The TriMAHCl mixtures having Al_2Cl_7 as the majority species ($\geq 64\%$) exhibited lower conductivity values (4-21 mS cm⁻¹) compared with the TriEAHCl mixtures (12–37 mS cm⁻¹). Even though the large ion size from the triethylammonium cation would be expected to reduce ion mobility even further than a trimethylammonium cation, the decrease in the number of available charge carriers via the AlCl₄⁻ dissociation reaction dominates.

The observed temperature-dependent conductivity behavior exhibited a classical linear Arrhenius behavior above room temperature (Figure S14), as observed in most ionic liquids. Generally, as the ionic liquids approach their glass transition temperatures the conductivity displays a significant negative deviation from linear behavior, consistent with glass-forming liquids, best described using the empirical Vogel-Tammann-Fulcher equation. 29,30 In the temperature range evaluated, the linear behavior may be explained by postulating the onset of an ionic solid-like conductance mechanism. Thus, there may occur a process whereby fluctuations in configurational entropy determine the relaxation time, and a process whereby individual ions undergo successive displacement in a semi-rigid lattice. 31 Both processes contribute to the conductance and hence to the slope of the $\ln \sigma$ vs. 1,000/T line, i.e., the activation energy.

The activation energy for $AlCl_4^-$ and $Al_2Cl_7^-$ conduction through the $AlCl_3$ /EMIMCI electrolytes varied based on the ions present in each mixture and their relative concentration. The electrolyte mixture with a 65% $AlCl_4^-$ and 35% $Al_2Cl_7^-$ showed the lowest activation energy (9.80 kJ mol $^{-1}$) compared with the mixtures with $AlCl_4^-$ as the majority species or $Al_2Cl_7^-$ as the majority species (14.35 and 11.64 kJ mol $^{-1}$), respectively) in the $AlCl_3$ /EMIMCI system. Interestingly, the 1.5:1 $AlCl_3$ /TriMAHCI electrolyte that exhibited a dense electrodeposited morphology compared with the rest presented a comparable activation energy for ionic conduction with the 1.6:1 $AlCl_3$ /TriEAHCI electrolyte and higher than the 1.8:1 $AlCl_3$ /EMIMCI electrolyte that exhibited a porous electrodeposited morphology. The activation energies calculated in combination with the ionic conductivities measured indicated that the high reversibility for plating and stripping is not a result of the ionic transport



within the electrolyte but point out that it may be an interfacial-controlled phenomenon.

Surface chemistry analysis on aluminum anodes

Progress in developing practical Al batteries has been hindered by multiple challenges associated with slow interfacial charge transport and sluggish electrochemical reactions at both the anode and the cathode. Among these challenges, the rapid formation of an irreversible, resistive, passivating Al₂O₃ film on the metal anode is considered the most difficult, because the oxidation reaction is thermodynamically favored, impedes stripping of Al³⁺, and reduces the battery working voltage. ^{26,32–34} Imidazolium-based IL electrolytes have been reported to overcome the anode passivation problem. 1,2,4 These electrolytes are believed to etch the passivating layer on the Al anode surface and form a new interfacial layer (the SEI) that simultaneously protects Al and regulates transport of ions to the electrode. Thus, we interrogated the surface chemistry of the Al anodes after 100 cycles of Al plating/stripping using SEM-EDS (Figures S15 and S16), followed by a more in-depth examination using X-ray absorption spectroscopy (XAS) and XPS. EDS analyses showed that the oxygen content present in the imidazolium-based electrolytes is twice as high as the oxygen present in the ammonium-based electrolytes after 100 cycles of plating and stripping (ending with a plating step), suggesting that etching of the Al₂O₃ layer is favored in the ammonium-based electrolytes.

The XPS high-resolution core scans provided insight into the nature of the bonds, i.e., that each element detected participates in the surface chemistry evolution of the Al anode as the number of cycles increases, going from a lower CE until it stabilizes at a higher value (Figure 5A–5I).

The anodes cycled with the 1.5:1 AlCl₃/TriMAHCl electrolyte were chosen for more in-depth studies because these anodes showed more planar, dense electrodeposited morphology compared with the other systems. In addition, Al foil as received was analyzed as a baseline (Figure S17). High-resolution and depth profiling (Figure \$18) measurements were performed on Al anodes transferred without air exposure between an Ar-filled glovebox and the ultrahigh vacuum XPS chamber. The O 1s and Al 2p signals reveal a significant difference between the surface layer after galvanostatic cycling in AlCl₃/TriMAHCl electrolyte vs. as-received Al foil. The O 1s spectra for the Al anode after 5 and 50 cycles show peaks assigned to Al₂O₃ $(528 \text{ eV})^{36}$ and AlO_x $(532.2 \text{ eV})^{37}$ compounds on the surface of the Al anode, suggesting oxidized Al metal, having a decrease in Al₂O₃ as the number of cycles increased and as the measurements were performed closer to the bulk. The Al 2p spectra show peaks assigned to Al-Cl (75.5 eV)³⁸ assigned to AlCl₄⁻ anions per surface-sensitive measurements on the Al anodes via soft XAS, Al₂O₃/AlO_x (74.5/74.7 eV), ³⁷ and Al-Al (72.1 eV). ³⁹ The peak in the Cl 2p spectra at 200 eV, attributed to Al-Cl, is assigned to AlCl₄⁻ anions per surface-sensitive measurements on the Al anodes via soft XAS.

Soft XAS was carried out as a complementary technique to the XPS high-resolution and survey scans. The XAS measurements were used to interrogate the surface of the Al anode where electrodes were cycled in either AlCl₃/TriMAHCl (1.5:1) or AlCl₃/TriMAHCl (2.6:1) electrolytes. The X-ray absorption near-edge structure (XANES) region of the XAS spectra of the two cycled anodes along with as-received Al metal foil predicted Al metal spectrum and an α -Al₂O₃ powder standard as shown in Figure 5J. Both recovered anode samples had similar profiles, consisting of a smaller initial edge jump at 1,559 eV as well as a primary edge at ca. 1,565 eV.



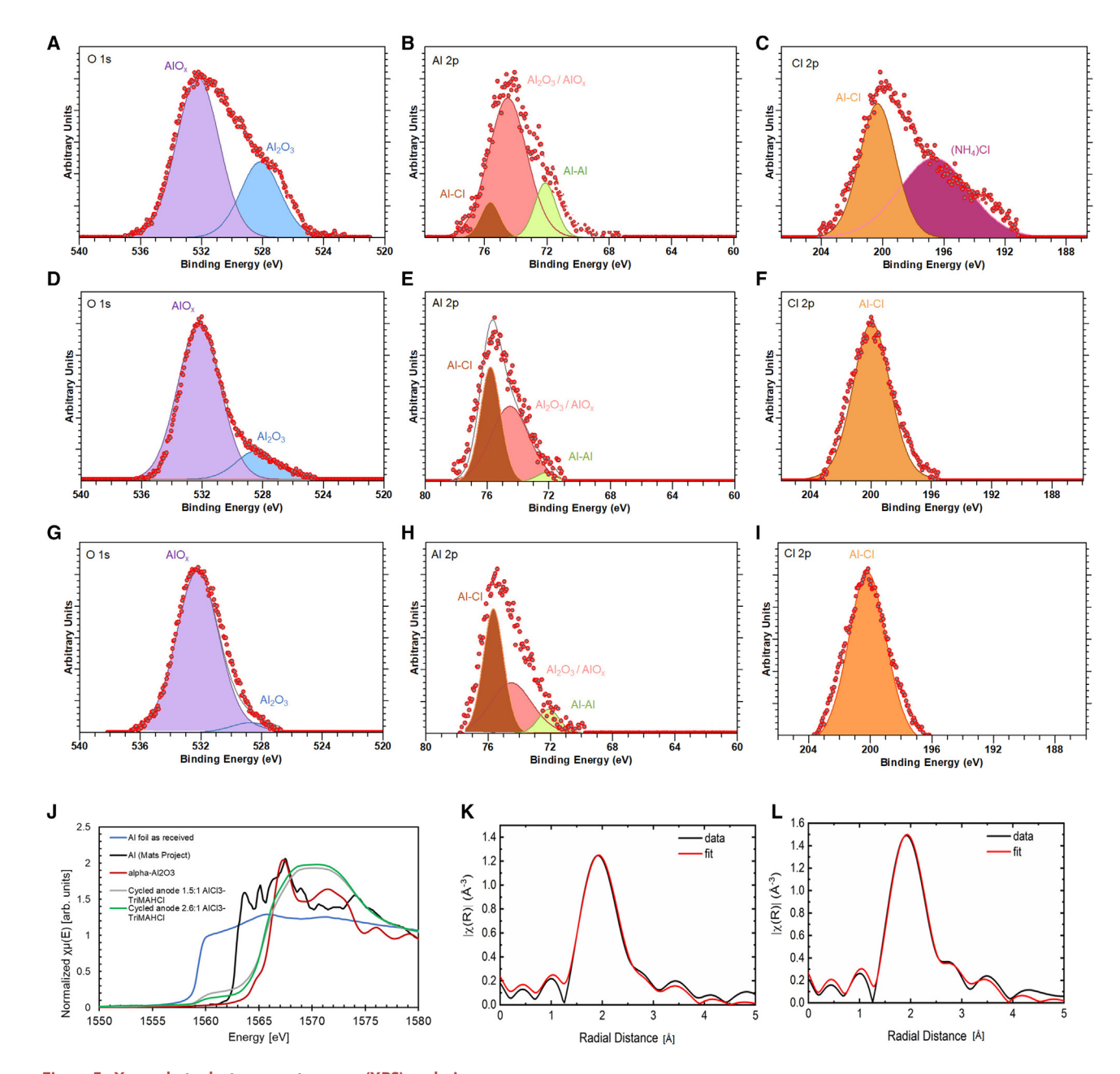


Figure 5. X-ray photoelectron spectroscopy (XPS) analysis

XPS analysis of Al anodes as a function of cycle number and depth on O 1s, Al 2p, and Cl 2p core levels, and k^2 -weighted $|\chi(R)|$ and corresponding EXAFS fit for Al anodes after 50 cycles of plating and stripping in AlCl₃/TriMAHCl electrolytes.

(A–C) cycle no. 5, (D–F) cycle no. 50, (G–I) cycle no. 50 after 127 min of Ar+ sputtering.

(J) XANES spectra of anode samples overlaid with Al foil as received, predicted Al metal spectrum, 35 and α -Al₂O₃ reference materials.

(K) 1.5:1 AlCl₃/TriMAHCl. (L) 2.6:1 AlCl₃/TriMAHCl. Fitting was performed using a two-phase model incorporating a theoretical model for the tetrachloroaluminate ion AlCl₄ and Al⁰. See also Tables S2 and S3; Figures S17–S19.

The initial edge jump at 1,559 eV is assigned to Al metal of the probed cycled electrode, while the higher edge energy is attributed to contributions from oxidized Al surface film species. It is noted that the sample spectra are significantly different from that of the α -Al₂O₃ standard, suggesting that such a crystalline phase is not present on the surface of the cycled Al anode. Moreover, the native alumina on the Al foil



as received does not correspond to the α -Al $_2$ O $_3$ standard. Jeurgens et al. ³³ reported that the surface energy of the amorphous metal oxide is often lower than that of the corresponding crystalline metal oxide. Consequently, up to a certain critical oxide-film thickness, a thin amorphous metal-oxide film on its metal substrate can be the stable modification with respect to the corresponding crystalline metal-oxide film on the same substrate, due to the relatively low surface and interfacial energies of the metal-substrate amorphous-oxide film system. Thus, upon exposure of a clean metal or semiconductor substrate to oxygen at relatively low temperatures (<500 K), often a thin (thickness <10 nm) passivating amorphous-oxide film is formed (this holds for Si, Ta, Nb, Al, Ge, Cr, and Te), whereas at higher temperatures thicker films develop and the resulting structure of the oxide film is in most cases crystal-line. ⁴⁰⁻⁴³ Thus, the broadening of the absorption spectrum is expected for the asreceived Al metal, given the presence of an amorphous metal-oxide layer, as a result of the enlarged distribution of neighboring atoms, which results in a high dispersion of crystal field values at the absorbing site. ⁴⁴

The Fourier transformed extended X-ray absorption fine structure (EXAFS) spectra of the 1.5:1 AlCl₃/TriMAHCl and 2.6:1 AlCl₃/TriMAHCl cycled samples were fitted using a model containing a tetrachloroaluminate (AlCl₄⁻) phase and an Al metal (Al⁰) phase (Figures 5K and 5L). The theoretical model for AlCl₄ was derived from the reported crystal structure of a lithium tetrachloroaluminate salt, 45 with an Al atom tetrahedrally surrounded by four chlorine atoms (Figure S19). The model utilizes three distinct photoelectron scattering paths: two single scattering paths corresponding to Al-Cl bonds with nominal interatomic distance of 2.10 Å and 2.14 Å, and a multiple scattering path at 3.90 Å, also detected in the high-resolution Al 2p spectra. Owing to the presence of Al⁰ in the samples as indicated by the XANES spectra, a structural model based on Al⁰ was also included as an additional phase. The coordination numbers were set to the crystallographic values for both AlCl₄ and Al⁰ phases. The experimental data fit well to the model, with R factors of 1.5 and 0.85 for anodes cycled in 1.5:1 AICl₃/TriMAHCl or 2.6:1 AICl₃/TriMAHCl electrolytes, respectively. For the AlCl₄ phase, the modeled interatomic distances are 2.00–2.03 Å for the Al–Cl single scattering paths and 3.78 Å for the multiple scattering path, which are ~0.12 Å shorter than the reported crystal structure. ⁴⁵ Al-Al bond distances in the Al⁰ phase were 2.83–2.86 Å, which is in excellent agreement with the reported 2.87 Å crystallographic value. 46 Full EXAFS fitting results are compiled in Table S3.

The results suggest that chloroaluminate (AlCl₄⁻) remains on the surface of the recovered Al anodes after 50 cycles. Considering the high-resolution XPS scans of the Al anodes as a function of cycling and depth (after 127 min of Ar⁺ sputtering), the Al₂O₃ at the surface is etched as a function of cycling, as is observed from the O 1s and Al 2p spectra, with an increasing concentration of AlCl₄⁻ present at the interface. Nonetheless, AlO_x remains present on the Al surface with AlCl₄⁻ even after 50 cycles where the CE values for Al plating and stripping have stabilized, which we speculate to be amorphous according to observations by Jeurgens et al.³³. The ion conduction of chloroaluminate species through the AlCl₄--rich layer is expected to be favored compared with the native alumina layer as it was observed through EIS measurements in Al symmetric cells (Figure S20). As assembled, the cell exhibited two constant phase elements: one corresponding to the native Al₂O₃ layer, "SL" for solid layer (capacitance value of 1 \times 10⁻⁶ F, kHz range) and a second one corresponding to the charge transfer resistance between the Al anode and the liquid electrolyte, "Al-LE" (capacitance value of 12 \times 10⁻⁵ F, Hz to mHz range). The capacitance values obtained through the equivalent circuit modeling for each semi-circle

Article



are in good agreement with values for surface layers and sample-electrode interface transport phenomena.⁴⁷ Analogously, the EIS spectrum after 50 cycles of cycling (after the CE values have reached equilibrium value and remain constant onward) was analyzed using the same equivalent circuit model. However, in this case, the first semi-circle is attributed to the AlCl₄--rich layer ("SEI"), confirmed by XAS and high-resolution XPS scans on the Al anode, showing a significantly lower impedance compared with the native alumina layer with improved charge transfer impedance. Thus, the beneficial interfacial layer in combination with the ease of charge exchange at the interface facilitates the kinetics of the electrodeposition process at the electrode-electrolyte interface, resulting in a more planar, dense electrodeposited morphology. In total, these observations suggest that the Lewis acidity of the electrolytes continuously etches the ionically resistive alumina layer, exposing the Al anode surface to the electrolyte that in turn becomes AlCl₄⁻-rich at the interface. However, there is an upper limit to the Lewis acidity (i.e., concentration of Al₂Cl₇ species) needed for this to occur. At high concentrations of Al₂Cl₇ (e.g., \geq 90%), corrosion of the components is observed (Figure S13).

Electrochemical behavior of aluminum vs. graphite full cells

As a first demonstration of the practical relevance of our findings, Al vs. graphite full cells were evaluated in galvanostatic cycling experiments using the electrolytes that showed the highest Al plating/stripping reversibility: AlCl₃/TriMAHCl (1.5:1) and AlCl₃/TriEAHCl (1.6:1), with cut-off potentials between 0.2 and 2.3 V (based on the electrochemical windows of the electrolytes; Figure S21 and Table S4). We note that although the ratios of AlCl₄⁻ to Al₂Cl₇⁻ are similar in these electrolytes and the electrolytes exhibit comparable Al plating/stripping reversibility, only the AlCl₃/TriMAHCl (1.5:1) supported stable long-term cycling of Al batteries, with more capacity fade when using AlCl₃/TriEAHCl (Figures 6A, S22, and S23). We conclude that the specific cation chemistry and physical properties play an important role in the solvation/desolvation characteristics of the electrolytes. We will take this aspect up in a follow-up study in which the effects of TriMAH⁺ and TriEAH⁺ size on the desolvation energy and formation of a cathode electrolyte interphase could provide insight into the cycling stability of both systems. In addition, the increase in reversibility in the first \sim 50 cycles is attributed to the anode interface, where the etching of the alumina surface layer occurs followed by the formation of an AlCl₄⁻-rich interfacial layer that enables high reversibility of Al plating and stripping.

Figure 6A reports the discharge capacity and CE of Al vs. graphite full cells cycled at a fixed current density of 335.4 mA g^{-1} (6 mA cm⁻²) with a graphite areal loading of ~12 mg cm⁻². Under these conditions, a specific discharge capacity of approximately 15 mAh g⁻¹ (based on the graphitic carbon mass in the cathode) and average CE of 97.65% are maintained for over 1,300 cycles in battery cells that use AICl₃/Tri-MAHCI (1.5:1) as electrolyte. While lower than the approximately 60 mAh g⁻¹ reported by Lin et al.² using a custom-fabricated nano-honeycomb graphene foam as the cathode, it is worth noting the large area loading of the cathodes used in Figures 6A and 6B (~12 mg cm⁻²). The reduced gravimetric capacity is attributed to the limited mesoscale transport (micrometers to millimeters) that can be captured in terms of resistance buildups associated with length effects on both ion and electron transport within thick electrodes, consequently decreasing the amount of effective active material. By lowering the areal loading of the graphite cathodes (\sim 2 mg cm $^{-2}$), gravimetric discharge capacity values between \sim 66 and 76 mA h g $^{-1}$ and CEs of \sim 95%–97% were observed at a current density of 6 mA cm⁻² when using 1.5:1 AlCl₃/TriMAHCl and 1.6:1 AlCl₃/TriEAHCl electrolytes (Figure S24). In addition, when lowering the discharge rates in the large area loading cathodes, higher



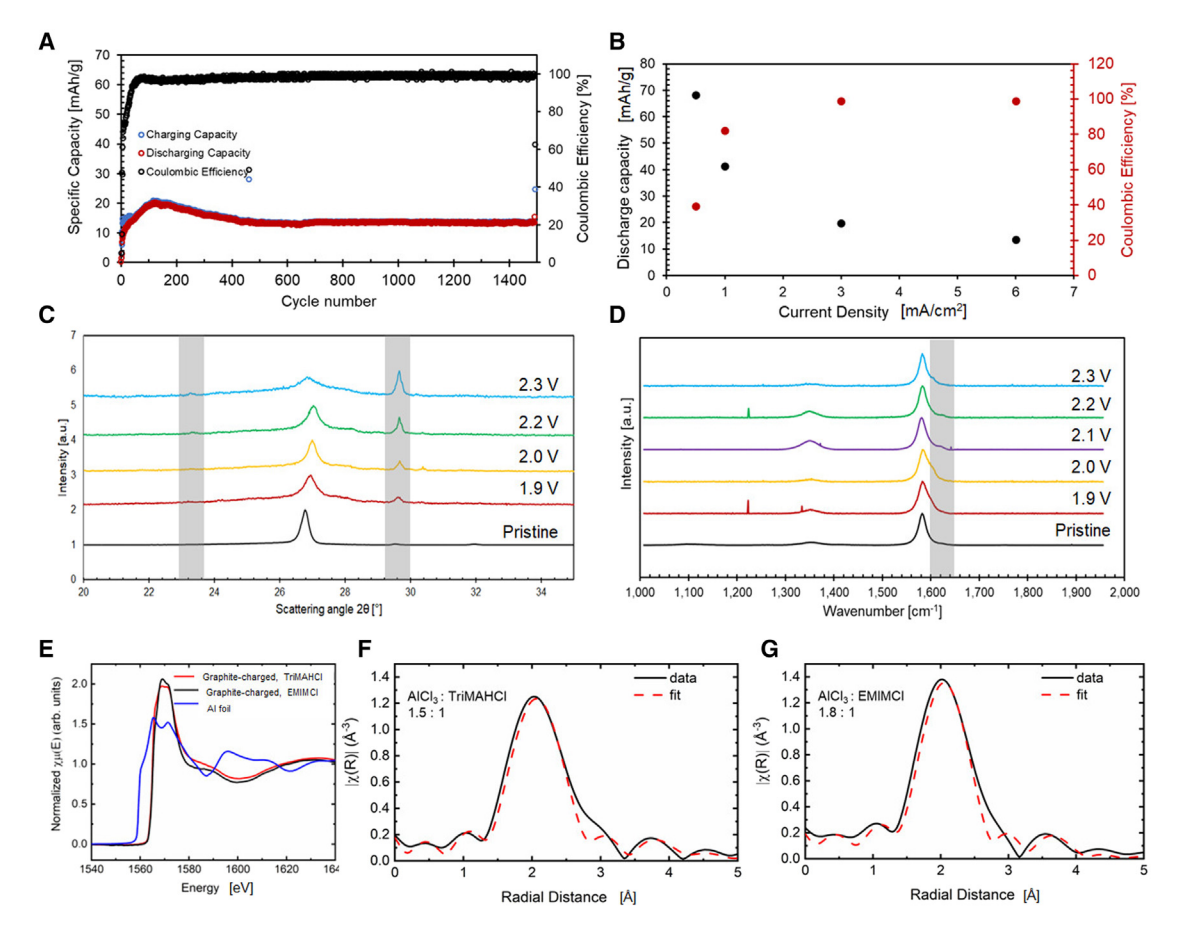


Figure 6. Electrochemical cycling behavior of Al-graphite cells and materials characterization of graphite cathode

(A) Long-term stability cycling test of an Al-graphite cell over 1,300 charging and discharging cycles at a current density of 335.4 mA $\rm g^{-1}$ (6 mA cm $^{-2}$) using 1.5:1 AlCl $_3$ /TriMAHCl as the electrolyte.

- (B) Specific discharge capacity and Coulombic efficiency as a function of current density of Al-graphite cells.
- (C) X-ray diffraction on graphite cathodes upon charging at 1 mA cm $^{-2}$ using 1.5:1 AlCl $_3$ /TriMAHCl as the electrolyte.
- (D) Raman on graphite cathodes upon charging at 1 mA cm $^{-2}$ using 1.5:1 AlCl $_3$ /TriMAHCl as the electrolyte.
- (E) XANES spectra of charged graphite cathodes and an Al foil standard.
- (F) k^2 -weighted $|\chi(R)|$ and corresponding EXAFS fit for graphite electrode charged in AlCl₃/TriMAHCI (1.5:1).
- (G) k^2 -weighted $|\chi(R)|$ and corresponding EXAFS fit for graphite electrode charged in AlCl₃/EMIMCI (1.8:1).

Fitting for (F) and (G) was performed using a theoretical model for the tetrachloroaluminate ion, $AlCl_4^-$. R factors for the fits were 3.1% and 3.7% for (F) and (G), respectively. The graphite area loading in (A) and (B) is \sim 12 mg cm⁻². See also Figures S22–S26 and Table S5.

discharge capacities are achievable, as seen in Figure 6B. However, the reversibility of the process is reduced significantly.

The X-ray diffraction (XRD) measurements on the cathodes after cycling are in good agreement with expectations for a stage-3 graphite intercalation compound (GIC) based on analysis of the diffraction patterns (Figure 6C). During the charging/anion intercalation process, aside from the (002) graphite peak, two new peaks arose at \sim 23.33° and \sim 29.63° 2 θ . The intensity of both peaks increased as the charging potential increased from 1.9 to 2.3 V. The most dominant peak is the (00n + 1) at 29.63° with a d spacing of 3.12 Å, and the second most dominant peak is the (00n +2) at 23.33° with a d spacing of 3.89 Å. By determining the ratio of the $d_{(00n+2)}/d_{(00n+1)}$ peak position and correlating these to the ratios of stage pure GICs, i.e., ideal cases, the most dominant stage phase of the observed GIC can be assigned. ^{48,49} We obtained a ratio of 1.24, meaning that the most dominant stage is 3, but there is a

Article



fraction of stage 4 according to the ratios reported by Zhang et al., 48 0.82 of stage 3 and 0.18 of stage 4. The intercalant gallery height (distance separating two graphite layers) was estimated to be $\sim\!5.22$ Å based on the diffraction patterns, suggesting that the AlCl₄ $^-$ anions with a comparable size ($\sim\!5.28$ Å) 50 are the most likely intercalant species.

Prior experimental² and theoretical work^{51,52} have proposed that a distorted tetrahedral geometry of AlCl₄⁻ is intercalated as opposed to a planar geometry,⁵³ given its higher thermodynamic stability. The distortion results from the van der Waals forces between the graphite layers, reducing the graphite interlayer distance by compressing the size of tetrahedral AlCl₄ and giving it a distorted geometry.⁵⁴ The Raman spectra collected on the same cathodes was also performed to probe chloroaluminate anion intercalation into graphite upon charge (Figure 6D). The graphite G band (~1,584 cm⁻¹) shows evidence of a right shoulder at ~1,605 cm⁻¹ upon anion intercalation, in good agreement with prior work by Lin et al. and Angell et al.^{2,6} We note that the initial G band remains largely intact, indicating that more hosting capacity exists in the cathode than is utilized in the battery discharge when using 1 mA cm⁻², as was observed when charging at a lower current density (0.5 mA cm⁻²), and achieving a larger gravimetric capacity (Figure 6B).

Both XRD and Raman measurements suggest that anion intercalation occurs upon charging and that $AlCl_4^-$ is the intercalation species in the graphite cathode. Nevertheless, to establish the identity of the intercalated species more conclusively, we performed XAS and Al-edge EXAFS measurements. XAS measurements were collected on graphite cathodes charged to 2.3 V where the electrolyte was either 1.5:1 $AlCl_3$ /TriMAHCl or 1.8:1 $AlCl_3$ /EMIMCl, for comparison. The XANES region of the XAS spectra of the charged samples as well as an Al metal foil standard is shown in Figure 6E. The edge energy of the charged samples was approximately 5.2 eV higher than the foil standard, indicating an oxidized Al species at the electrode. The sharp edge arises from Al 1s \rightarrow 3p transitions and is \sim 2 eV lower in energy than reported transitions edge energy for corundum Al_2O_3 .

The Fourier transformed EXAFS spectra of the charged graphite electrodes with the AlCl₃/TriMAHCl and AlCl₃/EMIMCl electrolytes are shown in Figures 6F and 6G. The spectra were successfully fit using a theoretical model derived from the reported crystal structure of a lithium tetrachloroaluminate salt, ³⁷ with an Al atom tetrahedrally surrounded by four chlorine atoms (Figure S25A). The model utilizes three distinct photoelectron scattering paths: two single scattering paths corresponding to Al–Cl bonds with nominal interatomic distance of 2.10 Å and 2.14 Å, and a multiple scattering path at 3.90 Å. The coordination numbers were set to the crystallographic values. The experimental data fit well to the model, with R factors of 3.1 and 3.7 for samples charged in AlCl₃/TriMAHCl (1.5:1) and AlCl₃/EMIMCl (1.8:1) electrolytes, respectively. Modeled interatomic distances of 2.09–2.10 Å for the single scattering paths and 3.90 Å for the multiple scattering paths are in excellent agreement with the reported crystal structure. Debye Waller disorder factor (σ^2) values were determined to range from 0.011 to 0.012 Å². Full EXAFS fitting results are presented in Table S5.

An alternative fitting model was also attempted that was derived from the crystal structure of a heptachloroaluminate salt. Heptachloroaluminate ions are composed of two AlCl₄ tetrahedra connected via a chlorine atom in a bent corner sharing configuration, with three Al–Cl bonds at 2.09–2.13 Å and a fourth, longer path at 2.22–2.26 Å (Figure S25B). Additional scattering paths are also predicted for non-bonding Al–Cl and Al–Al interactions at 3.74 Å and 3.69 Å, respectively.



Fitting of the experimental data to the heptachloroaluminate model resulted in a shift in interatomic radial distances of the first shell Al–Cl paths to lower values than predicted by the heptachloroaluminate crystal structure such that the average Al–Cl distance was 2.11 Å, which is the nominal first coordination shell distance for the tetrachloroaluminate structure. The Al–Cl and Al–Al paths also shifted from their nominal values by $\sim\!0.10$ Å to 3.86 Å, which is close to the radial distance of the multiple scattering path in ${\rm AlCl_4}^-$. Furthermore, if the interatomic distances were set to the nominal values from the published crystal structure, greater misfit was observed (Figure S26) when compared with the fits based on the tetrachloroaluminate structure (R factor of 6.3%–7.0% for heptachloroaluminate fitting model). These results provide evidence that the electroactive species at the cathode is the tetrachloroaluminate ion rather than the heptachloroaluminate ion. These results therefore motivate the design of cathode materials that allow fast diffusion of bulky ions, show reversible phase transformations, and maintain structural integrity upon cycling.

We report that low-cost electrolytes based on quaternary ammonium-based salts of broken symmetry can be designed with melting points below room temperature. By means of electrochemical, spectroscopic, and morphological analyses, we evaluate the critical role of each chloroaluminate species in Al electrochemical properties in batteries. We find that the reversibility of Al plating and stripping, the nature of the SEI it forms, and the morphological evolution during plating and stripping of Al depend sensitively and quantitatively on the ratio of $AlCl_4^-$ to $Al_2Cl_7^-$ ions in the electrolyte. The sensitivity stems from the dual role played by the ions in facilitating electroreduction at the Al-electrolyte interface and in etching the resistive native alumina surface layer that forms on the Al that prevents transport to the interface. A key finding is that provided the ratio of $AlCl_4^-$ to $Al_2Cl_7^-$ ions can be preserved in room-temperature electrolytes with broken cation symmetry, it is possible to achieve highly efficient plating and stripping of Al in cost-effective, quaternary ammonium-based electrolyte media.

We leverage the last discovery to create Al||graphite electrochemical cells and study them as platforms for achieving low-cost, long-duration storage of electrical energy. Galvanostatic charge-discharge measurements show that these cells demonstrate stable long-term cycling performance, particularly when AlCl₃/TriMAHCl (1.5:1) is used as electrolyte. The electrolyte molecular design approach presented here therefore offers a promising new route toward achieving low-melting-point electrolytes with the desired Lewis acidity for highly reversible Al electrodeposition and dissolution in secondary batteries.

EXPERIMENTAL PROCEDURES

Resource availability

Lead contact

Lynden A. Archer is the lead contact in this work, and can be contacted at the following email address: laa25@cornell.edu.

Materials availability

This study did not generate new unique reagents.

Data and code availability

Any additional information required to reanalyze the data reported in this paper is available from the lead contact (Lynden A. Archer, laa25@cornell.edu) upon reasonable request. This paper does not report original code.

Article



Electrolyte preparation

The chloroaluminate compounds were prepared by slowly adding appropriate amounts of anhydrous AlCl₃ to EMIMCI, TriMAHCI, TriEAHCI, TetraMACI, or tetraethylammonium chloride while stirring in a dry Ar-filled glovebox (<0.1 ppm H_2O , <1 ppm O_2).

Phase diagram construction

DSC measurements were carried out at different cooling/heating rates of 0.75° C min⁻¹, 1.5° C min⁻¹, 3° C min⁻¹, 4° C min⁻¹, 5° C min⁻¹, and 6° C min⁻¹. Exposure to moisture was minimized by drying the DSC pans in a vacuum oven at $\sim 120^{\circ}$ C for ≥ 8 h, with use of hermetic pans and sealing of the samples inside a dry Ar-filled glovebox (<0.1 ppm H₂O, <1 ppm O₂) immediately before the measurement was conducted. Freezing temperatures (T_{freeze}) were obtained upon solidification of the samples, starting with a cooling step for the compositions that form room-temperature molten salts. Alternatively, the compositions that are crystalline at room temperature were heated up to their melting temperature, followed by a cooling step.

²⁷Al nuclear magnetic resonance

Spectra were collected by using a Bruker AV400 NMR spectrometer at room temperature (298 K), BBFO broadband probe, and HD electronics console. The quantitative acquisition was performed (128 scans, 90° excitation, 1 s relaxation delay) with background suppression. The relative concentration determinations of $AlCl_4^-$ and $Al_2Cl_7^-$ species were performed in MestReNova version 14.2.1-27684 (Mestrelab Research) with a qNMR plug-in.

Electrode imaging and elemental mapping

The cross-section imaging of the AI electrode surface after cycling was conducted on Raith VELION FIB-SEM system with Au⁺ ion source. Before trenching, Pt was deposited onto the sample surface to protect the surface features. The cross-section images were taken using the SEM integrated into the system.

Cell assembly and electrochemical measurements

All cell assembly was conducted in a dry Ar-filled glovebox (<0.1 ppm H₂O, <1 ppm O₂), and all electrochemical tests were performed at room temperature (~25°C). Al plating/stripping CE measurements were carried out in Al (CE)||carbon cloth (WE) and Al symmetric coin cells (CR2032) using a Neware battery tester. 0.9525 cm (3 /8 inch) aluminum foil disks (25 µm thick, 99.45% metals basis, Alfa Aesar) were punched out and used as the anodes. 1.27 cm (1 /2 inch) plain carbon cloth disks (356 µm thick, 1071 HCB; Fuel Cell Store) were used as a substrate for Al galvanostatic electrodeposition/dissolution. One layer of fiberglass fiber filter paper GF-D (Whatman) was placed between the WE and CE with a diameter of 1.905 cm (3 /4 inch), and ~100 µL of electrolyte was poured before sealing. The amount of Al electrodeposited onto the carbon cloth in each step was fixed, followed by a stripping step. The percentage of Al stripped from the substrate electrode compared with the amount plated in the previous step represents the CE values reported in this work: CE [%] = (stripping capacity/plating capacity on substrate) × 100.

EIS measurements were collected in Al symmetric cells at room temperature using a potentiostat (BioLogic SP-200). The frequency range used was 7 MHz to 50 mHz, using 10 mV as the perturbation voltage, and three measurements were acquired per frequency. Al electrodes were used for ionic conductivity measurements. Equivalent circuit modeling was used to validate the analysis. The equivalent circuit used to



analyze the frequency-dependent transport phenomena was $Z_{u+LE} + Q_{SL/SEI}/Z_{SL/SEI} + Q_{CT, AI-LE}/Z_{CT, AI-LE}$, where Z_{u+LE} corresponds to the uncompensated and liquid electrolyte impedance, and $Q_{SL/SEI}$ and $Z_{SL/SEI}$ correspond to the constant phase element and ionic impedance of the solid layer/solid electrolyte interphase, respectively. $Q_{CT, AI-LE}$ and $Z_{CT, AI-LE}$ denote the constant phase element and impedance at the electrode/electrolyte interface (CT = charge transfer).

Full-cell measurements were carried out in Al (CE)||graphite (WE) coin cells (CR2032) using a Neware battery tester. 0.9525 cm (3 / $_8$ inch) aluminum foil disks (25 µm thick, 99.45% metals basis, Alfa Aesar) were punched out and used as the anodes. 1.27 cm (1 / $_2$ inch) plain carbon cloth disks (356 µm thick, 1071 HCB; Fuel Cell Store) were used as a substrate and current collector for the graphite cathodes. The graphite slurry consisted of 80 wt % artificial graphite powder (D $_{50}$ of 15 µm; MTI, item number Lib-CMSG), 10 wt % battery-grade carboxymethyl cellulose (CMC) binder, and 10 wt % deionized water. After coating the carbon cloth substrates with the graphite slurry, the electrodes were dried in an oven at 90°C for \geq 12 h before cell assembly. One layer of fiberglass fiber filter paper GF-D (Whatman) was placed between the anode and cathode, and ~100 µL of electrolyte was poured before sealing. The full cells were charged and discharged between the cut-off potentials of 2.3 and 0.2 V at a current density of ~330 mA g⁻¹ (6 mA cm⁻²), except for the cells used for XRD and Raman characterization (1 mA cm⁻²).

X-ray photoelectron spectroscopy measurements

A Surface Science Instruments SSX 100 was used for all XPS experiments. A custom-made airtight transfer holder was used to load the samples from a dry Ar-filled glove-box into the XPS instrument without air exposure. Survey scans used for the depth profiling used ion energy of 4 keV, a 10 mA current, a step size of 1 eV, a raster of 2 \times 4 mm, 150 V pass energy, and a spot size of 400 μ m. The high-resolution scans used a step size of 0.065 eV, resolution 2, while the rest of the parameters remained the same for the survey scans. All scans were quantified using Shirley backgrounds and sensitivity factors for O 1s, Al 2p, and Cl 2p in Casa XPS software. Core scans used a pass energy of 150 V and were calibrated using C–C bond energy at 285 eV. The following time steps and sequence were used to obtain surface chemistry measurements of the Al anode at the surface and near the bulk: 0 min, 2 min, 5 min, three measurements every 10 min of Ar sputtering, a high-resolution scan, three measurements every 30 min of Ar sputtering, a high-resolution scan, and five measurements every 60 min of Ar sputtering, for a total of \sim 13 h.

Structural changes of graphite cathodes upon intercalation

Graphite cathodes were collected after charging up to 1.9, 2.0, 2.1, 2.2, and 2.3 V from Al||graphite cells utilizing either AlCl₃/TriMAHCl (1.5:1) or AlCl₃/TriEAHCl (1.8:1) electrolytes. Cathodes were rinsed with anhydrous methanol, dried, and kept under an inert atmosphere prior to analysis.

XRD measurements were carried out using a Bruker D8 powder diffractometer (Cu K α 1.54 Å radiation, step size 0.0194577° between 20 and 35 2 θ degrees at 40 kV, 25 mA, a divergent beam slit of 1.0 mm, and a detector slit of 9 mm.

Raman spectra were collected using a WITec-Alpha 300R confocal Raman microscope. A 532 nm green laser was used at 2 mW, 1,200 L mm $^{-1}$ grating, spectral center at 1,500 cm $^{-1}$, 15 accumulations, and 30 s integration time.

Article



X-ray absorption spectroscopy measurements on Al anodes

Al K-edge XAS measurements were collected for Al anodes that were cycled in Al/ graphite cells utilizing either AlCl₃/TriMAHCl (1.5:1) or AlCl₃/TriMAHCl (2.6:1) electrolytes. Cathodes were rinsed, dried, and kept under inert atmosphere prior to analysis. The measurements were collected at the National Institute of Standards and Technology Partner Beamline 7-ID-1 (SST-1) at the National Synchrotron Light Source II, Brookhaven National Laboratory. Measurements were recorded under a 10^{-9} torr vacuum. In the pre-edge range (-200 to -20 eV below the edge), the incident beam energy was scanned using 5 eV steps. Across the edge (-20 to 30 eV), a 0.3 eV step size was used for enhanced resolution, and in the post-edge region (20-800 eV), a step of 0.05 \mathring{A}^{-1} was used. A 1 s acquisition time was used at each data point. Data were collected in total electron yield detection mode, and the X-ray spot size was approximately 300 \times 300 μ m. The energy was calibrated by setting the maximum of the first derivative of an Al foil spectra to 1,559 eV. XAS spectra were aligned, averaged, and normalized using Athena software. 56 The energy was calibrated by setting the maximum of the first derivative of an Al foil spectrum to 1,559 eV. The built-in AUTOBK algorithm was used to minimize background below $R_{bkq} = 1.2 \text{ Å}$. Normalized total electron yield (TEY) spectra were fit utilizing Artemis using theoretical models for $Al_0 \ AlCl_4^-$ created with FEFF6 based on reported crystal structures. 45,46,58,59 A k-range of 2.5–7.5 \mathring{A}^{-1} and Hanning window (dk = 1) were used as Fourier transform parameters, and fitting was performed using k² weighting. The R-space window was defined as 1.2–4.0 Å. The S_0^2 parameter was determined to be 0.88 from fitting an Al metal foil standard, and this term was applied to the fits to account for intrinsic losses in the electron propagation and scattering processes.

Intercalation species determination via X-ray absorption spectroscopy measurements

Cathodes were collected in the charged state (2.3 V) from Allgraphite cells utilizing either AlCl₃/TriMAHCl (1.5:1) or AlCl₃/EMIMCl (1.8:1) electrolytes. Cathodes were rinsed with anhydrous methanol, dried, and kept under an inert atmosphere prior to analysis. Al K-edge XAS measurements were collected at the National Institute of Standards and Technology Partner Beamline 7-ID-1 (SST-1) at the National Synchrotron Light Source II. Measurements were recorded under 10^{-7} Pa vacuum. In the pre-edge range (-200 to -20 eV below the edge), the incident beam energy was scanned using 5 eV steps. Across the edge (-20 to 30 eV), a 0.3 eV step size was used for enhanced resolution, and in the post-edge region (20–800 eV) a step of 0.05 ${\rm \AA}^{-1}$ was used. A 1 s acquisition time was used at each data point. Data collected in TEY detection mode were used for the XAS analysis, and fluctuations in the incident beam were accounted for via normalization using an Au-coated mirror located upstream of the sample. The energy was calibrated by setting the maximum of the first derivative of an Al foil spectrum to 1,559 eV. XAS spectra were aligned, averaged, and normalized using Athena.⁵⁵ The built-in AUTOBK algorithm was used to minimize background below $R_{bkg} = 1.2 \text{ Å}$. Normalized spectra were fit utilizing Artemis using theoretical models for AlCl₄⁻ and Al₂Cl₇⁻ created with FEFF6^{55,60} based on reported crystal structures of chloroaluminate salts. 45,61 A k-range of 2.5–7.5 \mathring{A}^{-1} and Hanning window (dk = 1) were used as Fourier transform parameters, and fitting was performed using k² weighting. The R-space window was defined as 1.2–4.0 Å. The S_0^2 parameter was determined to be 0.88 from fitting an Al metal foil standard, and this term was applied to the fits to account for intrinsic losses in the electron propagation and scattering processes.⁶²

The probe depth of the TEY XAS measurements must also be considered when interpreting the experimental results. ⁶³ During the X-ray absorption process a primary



core level electron is ejected, and the resulting core-excited atom can undergo relaxation either via emission of a fluorescent photon or via emission of an Auger electron. $^{2,13,56-58}$ Inelastic scattering of primary Auger electrons also occurs, resulting in emission of secondary electrons. In the TEY detection mode, the total number of emitted electrons (primary, Auger, secondary) from the sample are measured. The TEY probe depth increases with the core level energy being probed, with experimental studies indicating a maximum probe depth of 14.1 nm at 0.929 keV (Cu-L edge). At the Al-K edge (1.559 keV), the attenuation length of incident X-rays will be lower and the kinetic energy and inelastic scattering range of the Auger electrons will be higher, and consequently the probe depth of the TEY measurement in this experiment is anticipated to be greater than 14 nm. 56 While the staging mechanism of AlCl₄ intercalation in graphite is not completely understood, 32,58,64 average interlayer spacing from XRD has been reported between 4.55 Å and 5.70 Å, and a probe depth of 15 nm would correspond to 25–30 graphene layers in the intercalated graphite electrode.

SUPPLEMENTAL INFORMATION

Supplemental information can be found online at https://doi.org/10.1016/j.xcrp. 2023.101452.

ACKNOWLEDGMENTS

The authors would like to thank Ivan Keresztes for valuable discussions regarding NMR data acquisition and analysis. The cross-section imaging of Al electrodes was conducted in the MIT.nano Characterization Facilities by J.Z. using the Raith VELION FIB-SEM system and Themis STEM. The XAS and EXAFS measurements were conducted at Brookhaven National Laboratory by D.C.B., C.J., and D.A.F. This work was funded by the Center for Mesoscale Transport Properties, an Energy Frontier Research Center supported by the US Department of Energy, Office of Science, Basic Energy Sciences, under award no. DESC0012673. R.G.-M. acknowledges that this study is based on work supported by a Cornell Energy Systems Institute Post-Doctoral Fellowship. Cornell Center for Materials Research Shared Facilities are supported through the NSF MRSEC program (DMR-1719875). Cornell University NMR Facility is supported, in part, by the NSF through MRI award CHE-1531632.

AUTHOR CONTRIBUTIONS

Conceptualization, R.G.-M., J.Z., and L.A.A.; formal analysis, R.G.-M.; data curation and methodology, R.G.-M.; investigation, R.G.-M., J.Z., D.C.B., C.J., and D.A.F.; visualization, R.G.-M.; funding acquisition, R.G.-M., A.C.M., E.S.T., and L.A.A.; project administration, R.G.-M., J.Z., and L.A.A.; supervision: A.C.M., E.S.T., and L.A.A.; validation, R.G.-M.; writing – original draft, R.G.-M.; writing – review & editing. R.G.-M., J.Z., D.C.B., C.J., D.A.F., A.C.M., J.K.T., E.S.T., and L.A.A.

DECLARATION OF INTERESTS

R.G.-M, J.Z., and L.A.A. have filed a provisional US patent related to this work, application no. 63/321,747.

Received: November 7, 2022 Revised: March 29, 2023 Accepted: May 16, 2023 Published: June 6, 2023

Article



REFERENCES

- Jayaprakash, N., Das, S.K., and Archer, L.A. (2011). The rechargeable aluminum-ion battery. Chem. Commun. 47, 12610–12612. https://doi.org/10.1039/c1cc15779e.
- 2. Lin, M.-C., Gong, M., Lu, B., Wu, Y., Wang, D.-Y., Guan, M., Angell, M., Chen, C., Yang, J., Hwang, B.-J., and Dai, H. (2015). An ultrafast rechargeable aluminium-ion battery. Nature 520, 325–328. https://doi.org/10.1038/nature14340.
- 3. Zheng, J., Bock, D.C., Tang, T., Zhao, Q., Yin, J., Tallman, K.R., Wheeler, G., Liu, X., Deng, Y., Jin, S., et al. (2021). Regulating electrodeposition morphology in high-capacity aluminium and zinc battery anodes using interfacial metal–substrate bonding. Nat. Energy 6, 398–406. https://doi.org/10.1038/s41560-021-00797-7.
- Zhao, Q., Zachman, M.J., Al Sadat, W.I., Zheng, J., Kourkoutis, L.F., and Archer, L. (2018). Solid electrolyte interphases for high-energy aqueous aluminum electrochemical cells. Sci. Adv. 4, eaau8131. https://doi.org/10.1126/ sciadv.aau813131.
- Wilkes, J.S., Frye, J.S., and Reynolds, G.F. (1983). Aluminum-27 and carbon-13 NMR studies of aluminum chloridedialkylimidazolium chloride molten salts. Inorg. Chem. 22, 3870–3872. https://doi.org/10.1021/ ic00168a011.
- Angell, M., Pan, C.-J., Rong, Y., Yuan, C., Lin, M.-C., Hwang, B.-J., and Dai, H. (2017). High Coulombic efficiency aluminum-ion battery using an AlCl₃ -urea ionic liquid analog electrolyte. Proc. Natl. Acad. Sci. USA 114, 834–839. https://doi.org/10.1073/pnas. 1619795114
- Angell, M., Zhu, G., Lin, M.-C., Rong, Y., and Dai, H. (2020). Ionic liquid analogs of AlCl₃ with urea derivatives as electrolytes for aluminum batteries. Adv. Funct. Mater. 30, 1901928. https://doi.org/10.1002/adfm.201901928.
- Singh, R.K., and Schechter, A. (2018). Electrochemical investigation of urea oxidation reaction on beta Ni(OH)₂ and Ni/Ni(OH)₂. Electrochim. Acta 278, 405–411. https://doi. org/10.1016/j.electacta.2018.05.049.
- Cataldo Hernández, M., Russo, N., Panizza, M., Spinelli, P., and Fino, D. (2014). Electrochemical oxidation of urea in aqueous solutions using a boron-doped thin-film diamond electrode. Diam. Relat. Mater. 44, 109–116. https://doi. org/10.1016/j.diamond.2014.02.006.
- Yan, C., Lv, C., Jia, B.E., Zhong, L., Cao, X., Guo, X., Liu, H., Xu, W., Liu, D., Yang, L., et al. (2022). Reversible Al metal anodes enabled by amorphization for aqueous aluminum batteries. J. Am. Chem. Soc. 144, 11444–11455. https://doi.org/10.1021/jacs.2c04820.
- Brown, R.J.C., and Brown, R.F.C. (2000). Melting point and molecular symmetry.
 J. Chem. Educ. 77, 724. https://doi.org/10.1021/ed077o724.
- Yalkowsky, S.H. (2014). Carnelley's rule and the prediction of melting point. J. Pharmaceut. Sci. 103, 2629–2634. https://doi.org/10.1002/jps. 24034

- Wasserscheid, P., and Welton, T. (2007). Ionic Liquids in Synthesis, 2nd ed. (John Wiley & Sons, Ltd). https://doi.org/10.1002/ 9783527621194.
- Lazzús, J.A. (2012). A group contribution method to predict the melting point of ionic liquids. Fluid Phase Equil. 313, 1–6. https://doi. org/10.1016/j.fluid.2011.09.018.
- Lai, P.K., and Skyllas-Kazacos, M. (1988). Electrodeposition of aluminium in aluminium chloride/1-methyl-3-ethylimidazolium chloride. J. Electroanal. Chem. 248, 431–440. https://doi.org/10.1016/0022-0728(8)85103-9.
- Endres, F., Abbott, A., and MacFarlane, D.R. (2017). Electrodeposition from Ionic Liquids (John Wiley & Sons).
- 17. Mamantov, G., and Marassi, R. (2012). Molten Salt Chemistry (Springer).
- Nakayama, Y., Senda, Y., Kawasaki, H., Koshitani, N., Hosoi, S., Kudo, Y., Morioka, H., and Nagamine, M. (2015). Sulfone-based electrolytes for aluminium rechargeable batteries. Phys. Chem. Chem. Phys. 17, 5758– 5766. https://doi.org/10.1039/C4CP02183E.
- Kravchyk, K.V., Wang, S., Piveteau, L., and Kovalenko, M.V. (2017). Efficient aluminum chloride–natural graphite battery. Chem. Mater. 29, 4484–4492. https://doi.org/10.1021/ acs.chemmater.7b01060.
- Pang, Q., Meng, J., Gupta, S., Hong, X., Kwok, C.Y., Zhao, J., Jin, Y., Xu, L., Karahan, O., Wang, Z., et al. (2022). Fast-charging aluminiumchalcogen batteries resistant to dendritic shorting. Nature 608, 704–711. https://doi.org/ 10.1038/s41586-022-04983.
- Wen, X., Liu, Y., Xu, D., Zhao, Y., Lake, R.K., and Guo, J. (2020). Room-temperature electrodeposition of aluminum via manipulating coordination structure in AlCl₃ solutions. J. Phys. Chem. Lett. 11, 1589–1593. https://doi.org/10.1021/acs.jpclett.0c00256.
- Dalibart, M., Derouault, J., and Granger, P. (1982). Spectroscopic investigations of complexes between acetonitrile and aluminum trichloride. 2. Study of AICl₃ in acetonitrile mixtures of tetramethylammonium chloride, water, or nitromethane. Inorg. Chem. 21, 2241–2246. https://doi.org/10.1021/ic00136a023.
- Zheng, J., Garcia-Mendez, R., and Archer, L.A. (2021). Engineering multiscale coupled electron/ion transport in battery electrodes. ACS Nano 15, 19014–19025. https://doi.org/ 10.1021/acsnano.1c08719.
- Cui, J., Wang, A., Li, G., Wang, D., Shu, D., Dong, A., Zhu, G., Luo, J., and Sun, B. (2020). Composite sodium metal anodes for practical applications. J. Mater. Chem. A Mater. 8, 15399–15416. https://doi.org/10.1039/ DOTA024690
- Yu, H., Zeng, Y., Li, N.W., Luan, D., Yu, L., and Lou, X.W.D. (2022). Confining Sn nanoparticles in interconnected N-doped hollow carbon spheres as hierarchical zincophilic fibers for dendrite-free Zn metal anodes. Sci. Adv. 8, eabm5766. https://doi.org/10.1126/sciadv. abm5766.

- Elia, G.A., Marquardt, K., Hoeppner, K., Fantini, S., Lin, R., Knipping, E., Peters, W., Drillet, J.-F., Passerini, S., and Hahn, R. (2016). An overview and future perspectives of aluminum batteries. Adv. Mater. 28, 7564–7579. https://doi.org/10. 1002/adma.201601357.
- Qin, Q.-X., and Skyllas-Kazacos, M. (1984). Electrodeposition and dissolution of aluminum in ambient temperature molten salt system aluminum chloride N-butylpiridinium chloride. J. Electroanal. Chem. 168, 193–206. https://doi. org/10.1016/03648-1874(84)87098-7.
- Fannin, A.A., Floreani, D.A., King, L.A., Landers, J.S., Piersma, B.J., Stech, D.J., Vaughn, R.L., Wilkes, J.S., and Williams, J.L. (1984). Properties of 1,3-dialkylimidazolium chloride-aluminum chloride ionic liquids. 2. Phase transitions, densities, electrical conductivities, and viscosities. J. Phys. Chem. A 88, 2614–2621. https://doi.org/10.1021/ j150656a038.
- McEwen, A.B., Ngo, H.L., LeCompte, K., and Goldman, J.L. (1999). Electrochemical properties of imidazolium salt electrolytes for electrochemical capacitor applications.
 J. Electrochem. Soc. 146, 1687–1695. https:// doi.org/10.1149/1.1391827.
- Noda, A., Hayamizu, K., and Watanabe, M. (2001). Pulsed-gradient Spin-Echo ¹H and ¹⁹F NMR ionic diffusion coefficient, viscosity, and ionic conductivity of non-chloroaluminate room-temperature ionic liquids. J. Phys. Chem. B 105, 4603–4610. https://doi.org/10.1021/io004132g.
- Smedley, S.I. (1980). The Interpretation of Ionic Conductivity in Liquids (Springer US). https://doi.org/10.1007/978-1-4684-3818-5.
- Jeurgens, L.P.H., Sloof, W.G., Tichelaar, F.D., and Mittemeijer, E.J. (2002). Growth kinetics and mechanisms of aluminum-oxide films formed by thermal oxidation of aluminum. J. Appl. Phys. 92, 1649–1656. https://doi.org/ 10.1063/1.1491591.
- Jeurgens, L., Sloof, W., Tichelaar, F., and Mittemeijer, E. (2000). Thermodynamic stability of amorphous oxide films on metals: application to aluminum oxide films on aluminum substrates. Phys. Rev. B 62, 4707– 4719. https://doi.org/10.1103/PhysRevB. 62,4707.
- Snijders, P.C., Jeurgens, L.P.H., and Sloof, W.G. (2002). Structure of thin aluminium-oxide films determined from valence band spectra measured using XPS. Surf. Sci. 496, 97–109. https://doi.org/10.1016/S0039-6028(01) 01591-6.
- 35. Jain, A., Ong, S.P., Hautier, G., Chen, W., Richards, W.D., Dacek, S., Cholia, S., Gunter, D., Skinner, D., Ceder, G., et al. (2013). The Materials Project: a materials genome approach to accelerating materials innovation. APL Mater. 1, 011002.
- Turner, N.H., and Single, A.M. (1990). Determination of peak positions and areas from wide-scan XPS spectra. Surf. Interface Anal. 15, 215–222. https://doi.org/10.1002/sia. 740150305.



Cell Reports Physical Science Article

- Taylor, J.A. (1982). An XPS study of the oxidation of AlAs thin films grown by MBE. J. Vac. Sci. Technol. 20, 751–755. https://doi.org/ 10.1116/1.571450.
- McGuire, G.E., Schweitzer, G.K., and Carlson, T.A. (1973). Core electron binding energies in some Group IIIA, VB, and VIB compounds. Inorg. Chem. 12, 2450–2453.
- Kendelewicz, T., Petro, W.G., Babalola, I.A., Silberman, J.A., Lindau, I., and Spicer, W.E. (1983). Room temperature exchange reaction at the Al-InP (110) interface: soft x-ray photoemission studies. J. Vac. Sci. Technol. B 1, 623–627. https://doi.org/10.1116/1.582611.
- Doherty, P.E., and Davis, R.S. (1963). Direct observation of the oxidation of aluminum single-crystal surfaces. J. Appl. Phys. 34, 619–628. https://doi.org/10.1063/1.1729318.
- Revesz, A.G., and Fehlner, F.P. (1981). The role of noncrystalline films in the oxidation and corrosion of metals. Oxid. Metals 15, 297–321. https://doi.org/10.1007/BF01058831.
- 42. Fehlner, F.P. (1981). Low-Temperature Oxidation: The Role of Vitreous Oxides (Wiley).
- 43. Lawless, K.R. (1974). The oxidation of metals. Rep. Prog. Phys. *37*, 231–316. https://doi.org/ 10.1088/0034-4885/37/2/002.
- Gutiérrez, A., López, M.F., Hernando, A., and Rojo, J.M. (1997). X-ray-absorption spectroscopy study of the partial devitrification of amorphous Ni80B20 and the formation of amorphous nickel. Phys. Rev. B 56, 5039–5041. https://doi.org/10.1103/PhysRevB.56.5039.
- 45. Couch, T.W., Lokken, D.A., and Corbett, J.D. (1972). Crystal structures of tetratellurium(2+) tetrachloroaliuminate and heptachlorodialiuminate, Te₄²⁺(A|Cl₄⁻)₂ and Te₄²⁺(A|₂Cl₇⁻)₂. Inorg. Chem. 11, 357–362. https://doi.org/10.1021/ic50108a031.
- Cooper, A.S. (1962). Precise lattice constants of germanium, aluminum, gallium arsenide, uranium, sulphur, quartz and sapphire. Acta Crystallogr 15, 578–582. https://doi.org/10. 1107/S0365110X62001474.
- Irvine, J.T.S., Sinclair, D.C., and West, A.R. (1990). Electroceramics: characterization by impedance spectroscopy. Adv. Mater. 2, 132–138. https://doi.org/10.1002/adma. 19900020304.

- Zhang, X., Sukpirom, N., and Lerner, M.M. (1999). Graphite intercalation of bis(trifluoromethanesulfonyl) imide and other anions with perfluoroalkanesulfonyl substituents. Mater. Res. Bull. 34, 363–372. https://doi.org/10.1016/S0025-5408(99) 00035-5.
- Özmen-Monkul, B., and Lerner, M.M. (2010). The first graphite intercalation compounds containing tris(pentafluoroethyl) trifluorophosphate. Carbon 48, 3205–3210. https://doi.org/10.1016/j.carbon.2010.05.005.
- Takahashi, S., Koura, N., Kohara, S., Saboungi, M.-L., and Curtiss, L.A. (1999). Technological and scientific issues of room-temperature molten salts. Plasma lons 2, 91–105. https://doi. org/10.1016/S1288-3255(99)00105-7.
- Jung, S.C., Kang, Y.-J., Yoo, D.-J., Choi, J.W., and Han, Y.-K. (2016). Flexible few-layered graphene for the ultrafast rechargeable aluminum-ion battery. J. Phys. Chem. C 120, 13384–13389. https://doi.org/10.1021/acs. ipcc.6b03657.
- 52. Jung, S.C., Kang, Y.J., and Han, Y.K. (2016). Comments on Geometry and Fast Diffusion of AlCl₄ Cluster Intercalated in Graphite. Electrochim Acta 195, 158-165. https://doi. org/10.1016/j.electacta.2016.11.040.
- Wu, M.S., Xu, B., Chen, L.Q., and Ouyang, C.Y. (2016). Geometry and fast diffusion of AlCl₄ cluster intercalated in graphite. Electrochim. Acta 195, 158–165. https://doi.org/10.1016/j. electacta.2016.02.144.
- Bhauriyal, P., Mahata, A., and Pathak, B. (2017).
 The staging mechanism of AlCl₄ intercalation in a graphite electrode for an aluminium-ion battery. Phys. Chem. Chem. Phys. 19, 7980–7989. https://doi.org/10.1039/C7CP00453B.
- Henderson, G.S., de Groot, F.M.F., and Moulton, B.J.A. (2014). X-Ray absorption nearedge structure (XANES) spectroscopy. Rev. Mineral. Geochem. 78, 75–138. https://doi.org/ 10.2138/rmg.2014.78.3.
- Ravel, B., and Newville, M. (2005). Athena, artemis, hephaestus: data analysis for X-ray absorption spectroscopy using IFEFFIT.
 J. Synchrotron Radiat. 12, 537–541. https://doi. org/10.1107/S0909049505012719.

- Rehr, J.J., Mustre de Leon, J., Zabinsky, S.I., and Albers, R.C. (2002). Theoretical x-ray absorption fine structure standards. J. Am. Chem. Soc. 113, 5135–5140. https://doi.org/10. 1021/ja00014a001.
- Mairesse, G., Barbier, P., and Vignacourt, J.P. (1997). Lithium tetrachloroaluminate. Cryst. Struct. Commun. 6, 15–18.
- Rouxel, J. (1959). Réseau crystallin de l'oxychlorure de l'aluminum. C. R. Hebd. Seances Acad. Sci. 248, 810–812.
- Frenkel, A.I., Wang, Q., Marinkovic, N., Chen, J.G., Barrio, L., Si, R., Cámara, A.L., Estrella, A.M., Rodriguez, J.A., and Hanson, J.C. (2011). Combining X-ray absorption and X-ray diffraction techniques for in situ studies of chemical transformations in heterogeneous catalysis: advantages and limitations. J. Phys. Chem. C 115, 17884–17890. https://doi.org/10. 1021/jp205204e.
- 61. Lin, F., Liu, Y., Yu, X., Cheng, L., Singer, A., Shpyrko, O.G., Xin, H.L., Tamura, N., Tian, C., Weng, T.-C., et al. (2017). Synchrotron X-ray analytical techniques for studying materials electrochemistry in rechargeable batteries. Chem. Rev. 117, 13123–13186. https://doi.org/ 10.1021/acs.chemrev.7b00007.
- Newville, M., Boyanov, B.I., and Sayers, D.E. (1999). Estimation of measurement uncertainties in XAFS data. J. Synchrotron Radiat. 6, 264–265. https://doi.org/10.1107/ S0909049598018147.
- Erbil, A., Cargill, I., GS, Frahm, R., and Boehme, R.F. (1988). Total-electron-yield current measurements for near-surface extended x-ray-absorption fine structure. Phys. Rev. B 37, 2450–2464. https://doi.org/10.1103/PhysRevB. 37.2450.
- Pan C.-J., Yuan C., Zhu G., and Dai H. An operando X-ray diffraction study of chloroaluminate anion-graphite intercalation in aluminum batteries. Proc. Natl. Acad. Sci. USA 115, 5670–5675. https://doi.org/10.1073/ pnas.1803576115.
- Frazer, B.H., Gilbert, B., Sonderegger, B.R., and De Stasio, G. (2003). The probing depth of total electron yield in the sub-keV range: TEY-XAS and X-PEEM. Surf. Sci. 537, 161–167. https:// doi.org/10.1016/S0039-6028(03)00613-7.